Peak External Photocurrent Quantum Efficiency Exceeding 100% via MEG in a Quantum Dot Solar Cell

Octavi E. Semonin,[1,2] Joseph M. Luther,[1] Sukgeun Choi,[1] Hsiang-Yu Chen,[1] Jianbo Gao,[1,3] Arthur J. Nozik,[1,4]* Matthew C. Beard[1]*

Multiple exciton generation (MEG) is a process that can occur in semiconductor nanocrystals, or quantum dots (QDs), whereby absorption of a photon bearing at least twice the bandgap energy produces two or more electron-hole pairs. Here, we report on photocurrent enhancement arising from MEG in lead selenide (PbSe) QD-based solar cells, as manifested by an external quantum efficiency (the spectrally resolved ratio of collected charge carriers to incident photons) that peaked at 114 ± 1% in the best device measured. The associated internal quantum efficiency (corrected for reflection and absorption losses) was 130%. We compare our results with transient absorption measurements of MEG in isolated PbSe QDs and find reasonable agreement. Our findings demonstrate that MEG charge carriers can be collected in suitably designed QD solar cells, providing ample incentive to better understand MEG within isolated and coupled QDs as a research path to enhancing the efficiency of solar light harvesting technologies.

Third-generation solar energy conversion strategies attempt to improve the overall conversion efficiency by channeling excess photon energy normally lost to heat into usable free energy (1). One approach that has received considerable attention involves using quantum dots (QDs) to harvest that excess energy as additional charge carriers via multiple exciton generation (MEG) (2). A similar process occurs within bulk semiconductors (impact ionization); however, it requires 7 eV (180 nm) photons to produce one extra carrier in silicon (3) and therefore is incapable of impacting solar cell technologies. MEG has been shown to occur in isolated PbSe QDs at about twice the efficiency (4) observed in bulk PbSe, demonstrating that quantum confinement can increase the efficiency of the primary conversion step from a high-energy photon to multiple charge carriers (5–7). These studies used ultrafast transient absorption spectroscopy (TAS) to infer the number of electron-hole pairs produced per absorbed photon. Because of the indirect nature of the measurements, as well as the high photon fluences needed, there have been conflicting reports regarding the quantum yield determined from TAS (8–11). Furthermore, disagreements have arisen over the impact that MEG can have on solar energy conversion (7, 8). Therefore, confirming the TAS results and demonstrating that MEG can occur in a working solar cell without

external bias and under 1-sun solar intensities have been important research goals.

Two recent reports have shown progress toward these goals. Sambur et al. reported an internal quantum efficiency (IQE) greater than 100% in a photoelectrochemical cell consisting of a monolayer of PbS QDs strongly coupled to an atomically flat anatase surface (12), although the external quantum efficiency (EQE) and power conversion efficiency (PCE) were small due to

the limited absorption of the monolayer of QDs. Similarly, MEG has been invoked as an explanation for increased ultraviolet (UV) responsivity in PbS QD photoconductors (13) measured under a large external bias. However, showing an EQE greater than 100% without an applied bias has remained an open challenge. The EQE is a spectrally resolved photocurrent measured under zero external bias and represents the ratio of photocarriers collected by an external circuit to the number of incident photons at a given wavelength. This includes those photons that never reach the active layer due to reflection and absorption by inactive layers, so an EQE greater than 100% implies an IQE (restricted to photons absorbed by the active layer) that is possibly even greater. Here, we demonstrate a peak EQE as high as 114 ± 1% in a PbSe QD solar cell, providing definitive proof that MEG occurs in QDs.

Our approach toward this demonstration has been to form arrays of all-QD absorber layers that can be incorporated into suitable solar cell architectures such as Schottky barriers and *p-n* planar heterojunctions (used in this study). The assembly of the QD layer must address a multitude of issues resulting from the synthetic techniques used to produce the colloidal QDs before deposition. Long-chain organic ligands, such as oleic acid, are used in the synthesis of PbSe QDs to control growth kinetics, allow for stable colloidal dispersions, and passivate surface states through their metal-ligand chemistry. However, when present in QD films, they create a large barrier to electronic transport. Therefore, these ligands must be removed while maintaining or
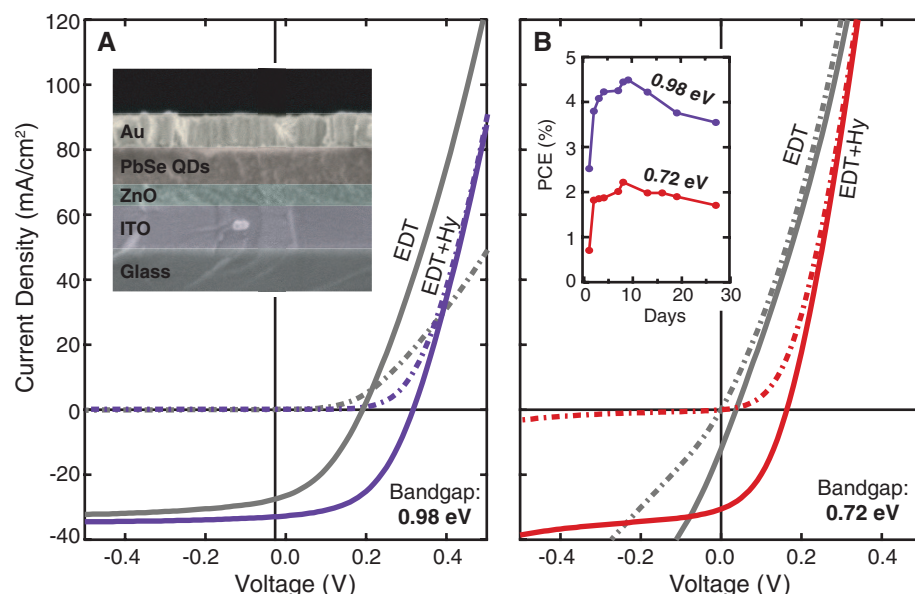

Fig. 1. Comparison of current-voltage characteristics under simulated AM1.5G illumination of devices assembled from EDT- and EDT+hydrazine–treated (**A**) small 0.98 eV QD films and (**B**) large 0.72 eV QD films. Solid lines correspond to 100 mW cm⁻² illumination, dot-dashed lines to dark conditions, purple to small QDs with EDT+hydrazine, red to large QDs with EDT+hydrazine, and gray to the respective QDs with EDT-only treatment. The upper inset to (A) displays a false-color cross-sectional SEM of a typical device. The inset to (B) shows the effect of aging (25 days under N₂) on mismatch-corrected PCE.

[1]National Renewable Energy Laboratory, 1617 Cole Boulevard, Golden, CO 80401, USA. [2]Department of Physics, University of Colorado, 390 UCB, Boulder, CO 80309, USA. [3]Department of Physics and Astronomy, University of Toledo, MS 111, Toledo, OH 43606, USA. [4]Department of Chemistry and Biochemistry, University of Colorado, 215 UCB, Boulder, CO 80309, USA

*To whom correspondence should be addressed. E-mail: arthur.nozik@nrel.gov (A.J.N.), matt.beard@nrel.gov (M.C.B.)

improving surface passivation and thereby controlling the electrical properties (*14*). Our most successful approach has been to treat the QDs with a short ligand that replaces the oleic acid during film formation. This is typically done in a layer-by-layer fashion (*15*), producing smooth pinhole-free layers.

The chemistry of QD surfaces has other important effects beyond improved conductivity. For example, we have studied MEG in coupled films of PbSe QDs using four distinct chemical treatments (*16*, *17*). Measured with ultrafast TAS,

the MEG efficiency showed variations that were not simply related to the ligand length. Films treated with 1,2-ethanedithiol (EDT) showed a reduced MEG efficiency—in agreement with IQE measurements of Schottky-junction PbSe QD solar cells constructed using EDT (*18*)—whereas films treated with hydrazine, methylamine, and ethanol preserved (to varying degrees) the MEG-enhanced photon-to-exciton quantum yield measured in colloidal dispersions (*17*). Early work (*19*) showed that hydrazine-treated PbSe QD films exhibit superior electron mobility on the

order of 1 cm² V⁻¹ s⁻¹, but no reports have successfully applied a hydrazine treatment to a QD solar cell. Conversely, although dithiol treatments such as EDT and benzenedithiol produce lightly doped QD films with much lower carrier mobilities of 0.0004 to 0.06 cm² V⁻¹ s⁻¹ (*20*), they have successfully produced PbSe or PbS QD layers for either Schottky-junction (*21*) or planar heterojunction (*22*, *23*) solar cells.

We used both EDT and hydrazine in a sequential manner during deposition of the QD film used in the solar cells studied here. Device fabrication started with a transparent glass/indium tin oxide (ITO) superstrate, and we successively deposited a 40- to 60-nm ZnO layer, a 50- to 250-nm QD layer, and a thermally evaporated gold anode [scanning electron microscopy (SEM) cross section in Fig. 1A inset]. We used layer-by-layer (LbL) EDT treatment (*15*) to deposit the majority of the QD film, followed by LbL deposition of ~30 nm of QDs, using 1 M hydrazine in acetonitrile to treat instead of EDT (*24*). We observe that this mild hydrazine treatment does not result in an *n*-type QD film.

Figure 1 compares the current-voltage characterization of typical QD solar cells prepared using the EDT+hydrazine treatment to EDT-only prepared devices. For all QD sizes tested, using hydrazine yields a dramatic improvement in all of the performance parameters (open circuit voltage, short circuit current, fill factor, series resistance, and shunt resistance). We also note the elimination of the crossover between the light and dark currents in forward bias (Fig. 1A), indicating an ohmic anode contact (*25*). We observed a beneficial aging effect on the solar cell performance under oxygen- and water-free nitrogen storage conditions, and thus our EQE data were collected after the initial rise in performance. This aging could be related to desorption of hydrazine reported for similarly treated PbSe films (*19*, *26*). The inset to Fig. 1B shows the mismatch-corrected PCE as a function of the device age, with a best PCE of 4.5% for the 0.98 eV device after 8 days. Previous reports for QD solar cells have reached 4.5% using larger bandgap PbSe QDs, and 6% using PbS QDs (*27*, *28*). We have found that our hydrazine treatment technique is effective with both PbSe and PbS QDs and also that other molecules—such as formic acid, 3-mercaptopropionic acid, methylamine, and ethanol—can be used in place of hydrazine, with comparable benefits to the current-voltage characteristics. For the MEG studies, the hydrazine-treated devices allowed for the use of larger QD sizes with smaller bandgaps, facilitating the ability to study high-energy photons relative to the bandgap. Additionally, the ZnO/PbSe interface produces an *n-p* heterojunction that facilitates extraction of charge carriers produced from high-energy photons (those capable of undergoing MEG), which are mostly absorbed in the first 50 nm of the PbSe film (see fig. S1).

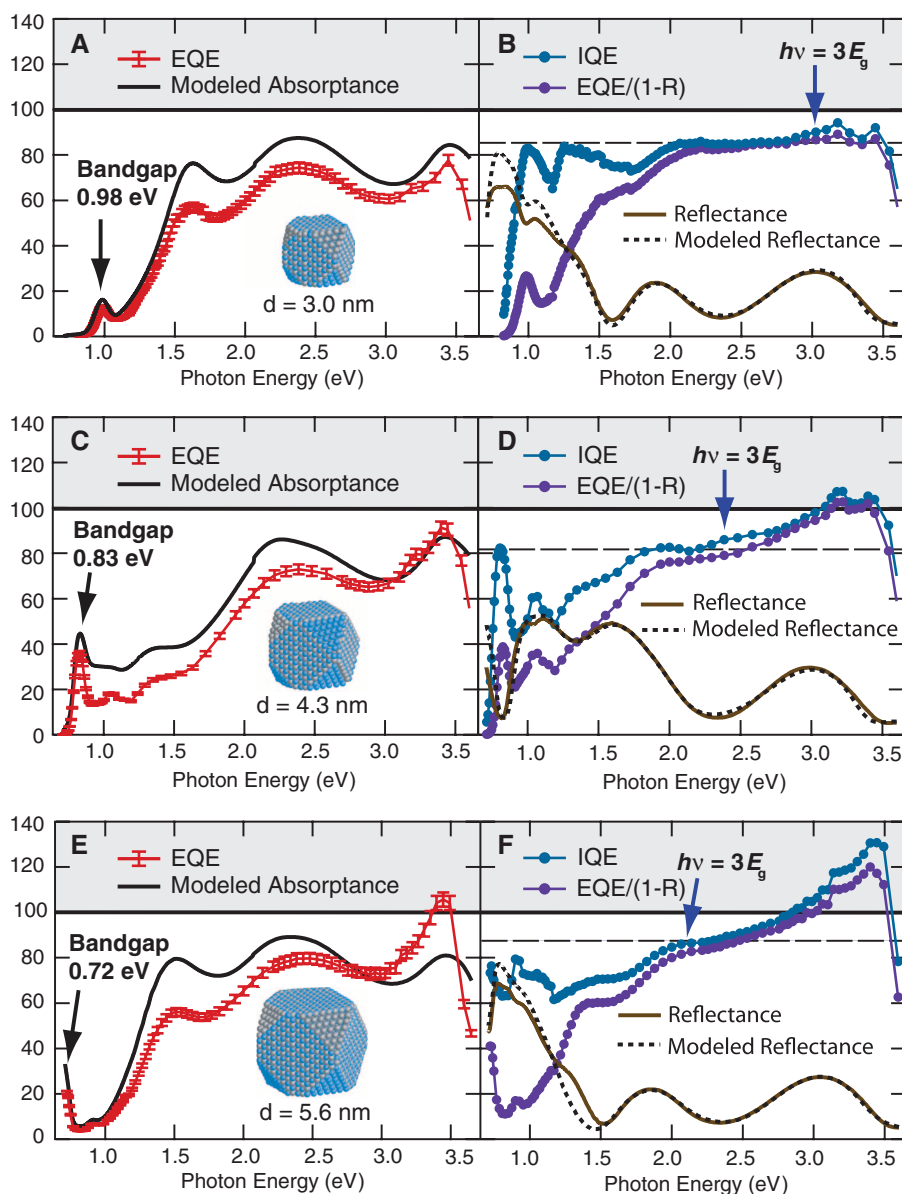Figure 2 displays full-spectrum EQE (red) and reflection (brown) profiles for three typical

Fig. 2. Red curves are the measured EQE for three representative QD solar cells made from PbSe QDs with indicated diameters and associated bandgaps of (**A** and **B**) 0.98 eV, (**C** and **D**) 0.83 eV, and (**E** and **F**) 0.72 eV. We estimate the uncertainty of these EQE curves to be ~3% (see SOM text for details). We plot the modeled absorptance of the QD plus ZnO layers [(A), (C), and (E), solid black] (see fig. S3 for all layers) and measured reflectance [(B), (D), and (F), brown]. The IQE is determined either by $EQE/[1 − R]$ (purple curves) or by EQE/A (blue curves), where A is the modeled absorptance of the PbSe plus ZnO layers. The modeled reflectance is shown as the dashed black line. For each data set, the IQE begins to rise at a photon energy of about 3 times the bandgap, E_g, peaking higher for decreasing E_g.

devices, with QD size-dependent bandgaps (E_g) of 0.98 eV (Fig. 2, A and B), 0.83 eV (Fig. 2, C and D), and 0.72 eV (Fig. 2, E and F). At the lowest photon energies ($h\nu$) the first exciton absorption peak is clearly visible, and optical mode buildup is responsible for the observed oscillations at higher photon energies. Despite reflection and absorption by the glass, ITO, and ZnO layers before the incident light reaches the QD layer, the device with the largest sized QDs (E_g = 0.72 eV) exhibited an EQE of 106 ± 3% at 3.44 eV photon energy (λ = 360 nm) (Fig. 2E). We determined the IQE from the EQE in two ways. First, because all photons not absorbed within the solar cell are reflected, to first order, the IQE is equal to the EQE divided by $[1 - R(h\nu)]$, where $R(h\nu)$ (Fig. 2, brown) is the reflectance at a photon energy of $h\nu$ (measured using an integrating sphere to include diffuse reflectance). The $EQE/(1 - R)$ ratio (Fig. 2, purple) represents the lower limit to the IQE, as it is not corrected for light absorbed by other layers that do not contribute to the photocurrent. For example, the $EQE/(1 - R)$ ratio decreases for photon energies less than 2 eV because of ITO absorption in that near-infrared spectral region. To account for such losses, we used a second approach. We determined the absorptance and reflectance of each layer by applying an optical model (18) with index of refraction (n) and extinction coefficient (k) determined by ellipsometry for each component layer (see SOM text for ellipsometry and modeling details, and fig. S2 for plotted refractive indices).

In the UV-visible spectral region of most interest, the modeled reflectance (Fig. 2, dashed black) and the measured reflectance (brown) agree very well and are fairly insensitive to QD and ZnO layer thicknesses because in this region the photons are all absorbed within 50 to 100 nm of the ZnO/QD interface. We show how the IQE and calculated R vary in fig. S4 for different layer thicknesses. The IQE is determined by normalizing the EQE to the calculated absorptance (Eq. 1):

$$IQE = \frac{EQE}{A} \qquad (1)$$

where we include the absorptance of both the ZnO and the PbSe layers $A = A_{PbSe} + A_{ZnO}$. The IQE differs from $EQE/(1 - R)$ only slightly in the UV-visible region but more in the longer-wavelength region (where absorption by ITO does not yield photocurrent). The IQE curves exhibit short-circuit collection yields of around 85% until the photon energy surpasses the MEG threshold, after which the IQE rises to a peak efficiency of 130% in the 0.72 eV QDs, 108% in the 0.83 eV QDs, and 98% in the 0.98 eV QDs. The glass, ITO, and ZnO begin to absorb large quantities of light at photon energies greater than 3.5 eV, and the EQE and IQE drop sharply. Enhanced interfacial recombination of carriers at these high photon energies may also contribute to the drops in EQE and IQE, as is typical in conventional solar cells.

To verify the accuracy of our measurement apparatus, we measured the EQE of a Thorlabs FDS-100-CAL calibrated silicon photodiode and observed excellent agreement with the commercially provided NIST-traceable calibration (fig. S5). In an effort to reduce the ~3% uncertainty associated with the full-spectrum EQE determination, we then optimized our apparatus for measurement in the near-UV where the EQE peaks and applied it to three sets of PbSe QDs with bandgaps near 0.72 eV (Fig. 3A). The best device measured had a peak EQE of 107.5 ± 0.6%, which increased to 114 ± 1% with the application of a 70-nm film of MgF$_2$ to act as an antireflection coating on the glass. Of the 18 devices made, all achieved EQE values over 95% and 15 exhibited EQE greater than 100%. The measurement uncertainty ranged from ±0.6 to ±1% at the peak. The variations result from slightly different film thicknesses, degree of ligand re-

moval, surface passivation, and other uncontrolled variables.

There are several reports of IQE greater than 100% and one report of an EQE greater than 100% based on impact ionization in bulk semiconductor devices. Canfield *et al.* (3) reported a peak EQE of 128% at a photon energy of 7.7 eV in a bulk silicon photodiode, corresponding to a relative photon energy of 7 E_g. For bulk silicon-based solar cells, the photon energy threshold for carrier multiplication occurs around 3.9 eV, or 3.5 E_g (3), and at 2.8 eV, or 4.1 E_g, in germanium (29). Here, the onset for the 0.72 eV bandgap QDs was ~2 eV or ~2.8 E_g.

To further assess the MEG efficiency, η_{MEG} (7), in Fig. 3B, we plotted the IQE curves from Fig. 2 versus $h\nu/E_g$ (the photon energy normalized to the bandgap of the QD). Some researchers suggest (8) that to assess the fundamental photophysics of the MEG process, the quantum efficiency should be plotted on an absolute photon energy basis (see fig. S6 for a plot on the absolute photon energy basis). However, we argue (7) that the $h\nu/E_g$ basis is more appropriate for understanding the fundamental competition between hot-carrier cooling and the MEG relaxation channel, as well as the practical utility for solar energy conversion. The slope of such plots is also proportional to the number of additional excitons created per bandgap of photoexcitation. Regarding this issue, we find it notable that the IQE curves for different sized QDs are so similar on the $h\nu/E_g$ basis, indicating that the ability to convert high-energy photons to multiple excitons is mainly determined by the excess energy relative to the threshold energy required to create an exciton.

We compared photocurrent results to spectroscopic results reported in previous literature in Fig. 3C. We found a clear trend in peak IQE values (blue circles) that agrees well with spectroscopic measurements (hollow triangles and squares), despite a difference of about 15% due to intrinsic
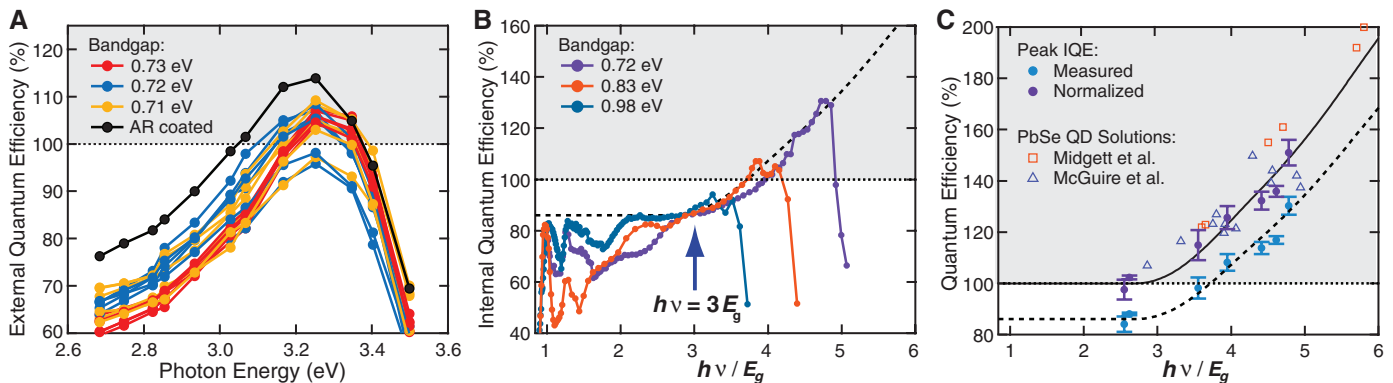

Fig. 3. (**A**) EQE peaks for 18 independent devices made with QD bandgaps of 0.71 eV (yellow), 0.72 eV (blue), and 0.73 eV (red), as well as a device with an antireflective coating (black). (**B**) Collected IQE curves versus the ratio of photon energy to bandgap, $h\nu/E_g$, for the three QD sizes in Fig. 2. The dashed curve is a previously published fit for colloidal QDs using the model described in (7), whereas here it has been normalized for intrinsic losses in the cell due to recombination. (**C**) Peak IQE values for seven different QD sizes. We plot the peak IQE values corrected for intrinsic losses in the solar cell (estimated at ~15%). Error bars are the propagated uncertainty of 5 to 30 measurements at the given wavelength of both the reference detector and the test solar cell. The solid black curve is the original fit to colloidal QDs from (7), whereas the dashed curve is the same as in (B). The hollow triangles and squares represent ultrafast transient absorption measurements of PbSe QD solutions taken from (9) and (10), respectively.

photocurrent losses. The IQE of the two devices using large bandgap QDs (1.35 eV and 1.48 eV) exhibited peak quantum efficiencies consistent with the 85% plateau for photon energies below the MEG threshold; thus, we estimate the intrinsic photocurrent losses at ~15%. We attribute these losses to electron-hole recombination before carrier separation and collection as photocurrent and therefore normalize the measured IQE to these values, yielding the purple circles in Fig. 3C. These values compare well with a model (7) that accounts for a competition between MEG and hot-exciton cooling (Fig. 3C, solid black curve, dashed curve normalized as above). Finally, we applied a least-squares linear fit of a normalized version of the same model (24) to the IQE for the 0.72 eV solar cell in Fig. 3B, yielding $\eta_{MEG} = 0.62 \pm 0.1$, and an MEG onset threshold E_{th} (Eq. 2)

$$E_{th} = \left(1 + \frac{1}{\eta_{MEG}}\right)E_g = (2.61 \pm 0.03)E_g \quad (2)$$

indicating quantitative agreement with spectroscopic measurements. We believe this result constitutes incontrovertible evidence that MEG is more efficient in PbSe QDs than in bulk PbSe, which exhibits a MEG efficiency of only 0.31 and a corresponding onset of 4.22 E_g (7, 30). To estimate the impact of MEG on the PCE, we integrated the 0.72 eV device IQE in excess of the baseline 85% (fig. S7, shaded region) against the AM1.5G solar spectrum. We estimate that ~1 mA cm^{-2}, or ~4%, of the total photocurrent arises from MEG, consistent with previous estimates based on TAS measurements of MEG in colloidal QDs (7). Bulk Si photovoltaic cells could only benefit by <1% from impact ionization, and Si$_{1-x}$Ge$_x$ alloys could benefit by at most 2% (29).

The useful effects of our hydrazine treatment allow multiple carriers produced by MEG to be efficiently collected in a solar cell made from

electronically coupled QDs. To have the largest impact on solar energy conversion efficiency, the MEG onset would have to be close to twice the bandgap, which could lead to a bonus photocurrent contribution as high as 30% (1, 7). The challenge is to learn how to further improve the MEG-enhanced quantum efficiency and this will necessarily involve maximizing the MEG kinetics by chemical, dimensional, or architectural means, while also limiting the inelastic, phonon-mediated exciton cooling rates. Carbon nanotubes (31, 32) and PbSe nanorods (33) have shown promising results in this direction. Our findings are a first step toward breaking the single junction Shockley-Queisser limit (34) of present-day first and second generation solar cells, thus moving photovoltaic cells toward the third-generation regime.

References and Notes

1. M. C. Hanna, A. J. Nozik, *J. Appl. Phys.* **100**, 074510 (2006).
2. A. J. Nozik, *Physica E* **14**, 115 (2002).
3. L. R. Canfield, R. E. Vest, R. Korde, H. Schmidtke, R. Desor, *Metrologia* **35**, 329 (1998).
4. The MEG efficiency, η_{MEG}, is related to the number of additional excitons generated per additional bandgap of energy carried by an absorbed photon after the threshold photon energy for MEG is passed.
5. J. A. McGuire, M. Sykora, J. Joo, J. M. Pietryga, V. I. Klimov, *Nano Lett.* **10**, 2049 (2010).
6. C. Delerue, G. Allan, J. J. H. Pijpers, M. Bonn, *Phys. Rev. B* **81**, 125306 (2010).
7. M. C. Beard et al., *Nano Lett.* **10**, 3019 (2010).
8. G. Nair, L. Y. Chang, S. M. Geyer, M. G. Bawendi, *Nano Lett.* **11**, 2145 (2011).
9. J. A. McGuire, J. Joo, J. M. Pietryga, R. D. Schaller, V. I. Klimov, *Acc. Chem. Res.* **41**, 1810 (2008).
10. A. G. Midgett, H. W. Hillhouse, B. K. Huges, A. J. Nozik, M. C. Beard, *J. Phys. Chem. C* **114**, 17486 (2010).
11. M. C. Beard, *J. Phys. Chem. Lett.* **2**, 1282 (2011).
12. J. B. Sambur, T. Novet, B. A. Parkinson, *Science* **330**, 63 (2010).
13. V. Sukhovatkin, S. Hinds, L. Brzozowski, E. H. Sargent, *Science* **324**, 1542 (2009).
14. D. V. Talapin, J. S. Lee, M. V. Kovalenko, E. V. Shevchenko, *Chem. Rev.* **110**, 389 (2010).
15. J. M. Luther et al., *ACS Nano* **2**, 271 (2008).
16. J. M. Luther et al., *Nano Lett.* **7**, 1779 (2007).
17. M. C. Beard et al., *Nano Lett.* **9**, 836 (2009).
18. M. Law et al., *Nano Lett.* **8**, 3904 (2008).
19. D. V. Talapin, C. B. Murray, *Science* **310**, 86 (2005).
20. Y. Liu et al., *Nano Lett.* **10**, 1960 (2010).
21. J. M. Luther et al., *Nano Lett.* **8**, 3488 (2008).
22. K. S. Leschkies, T. J. Beatty, M. S. Kang, D. J. Norris, E. S. Aydil, *ACS Nano* **3**, 3638 (2009).
23. J. J. Choi et al., *Nano Lett.* **9**, 3749 (2009).
24. See the supporting material on *Science* Online for a complete description of materials synthesis; device fabrication, characterization, and modeling; and details of the MEG model used in Fig. 3.
25. J. Gao et al., *Nano Lett.* **11**, 1002 (2011).
26. R. Y. Wang et al., *Nano Lett.* **8**, 2283 (2008).
27. W. Ma et al., *ACS Nano* **5**, 8140 (2011).
28. J. Tang et al., *Nat. Mater.* **10**, 765 (2011).
29. M. Wolf, R. Brendel, J. H. Werner, H. J. Queisser, *J. Appl. Phys.* **83**, 4213 (1998).
30. J. J. H. Pijpers et al., *Nat. Phys.* **5**, 811 (2009).
31. N. M. Gabor, Z. H. Zhong, K. Bosnick, J. Park, P. L. McEuen, *Science* **325**, 1367 (2009).
32. S. J. Wang, M. Khafizov, X. M. Tu, M. Zheng, T. D. Krauss, *Nano Lett.* **10**, 2381 (2010).
33. P. D. Cunningham et al., *Nano Lett.* **11**, 3476 (2011).
34. W. Shockley, H. Queisser, *J. Appl. Phys.* **32**, 510 (1961).

Growth of Uniformly Oriented Silica MFI and BEA Zeolite Films on Substrates

Tung Cao Thanh Pham, Hyun Sung Kim, Kyung Byung Yoon*

Applications of zeolite films benefit from alignment of the integrated channels, but methods for film growth have nearly always introduced orientational randomization in the direction normal to the substrate. We now report facile methods to grow silicalite-1 films and pure silica beta zeolite films on substrates with straight or sinusoidal channels positioned uniformly upright at a thickness of up to 8 micrometers. Precise gel compositions and processing temperatures are critical to promote secondary growth on pre-formed oriented crystal monolayers while suppressing self-crystallization in the bulk medium. Preliminary results highlight the potential of these uniformly oriented films in the nonlinear optical response and separation of xylene isomers.

Zeolites are aluminosilicates with angstrom-scale pores and channels in their crystal lattice. When grown as continuous films on various substrates, they function as molecular sieve membranes (1–13) and platforms for second-order nonlinear optical (2-NLO) mixing (14–16), among other applications (17–20). In these contexts, optimal performances would be expected when the channel directions were uniformly oriented normal to the substrate planes

from the top to the bottom of the films. However, despite great effort over the past three decades (1–13, 21, 22), uniformity in the channel orientation of zeolite films has not been achieved.

For example, silicalite-1 (SL) is a pure silica MFI (23) zeolite with 5.5 × 5.1 Å–sized elliptical channels running along the a axis in a sinusoidal manner and 5.6 × 5.3 Å–sized elliptical channels running straight along the b axis (Fig. 1, A and B) (24). Previous attempts to grow it as a continuous film with the sinusoidal (a-axis) and straight (b-axis) channels pointing perfectly normal to the substrates have not been successful (3, 6–10, 12). Another zeolite, beta (BEA) (23), adopts a truncated bipyramidal shape, with 6.6 × 6.7 Å channels running straight along the a (or b) axis and

Korea Center for Artificial Photosynthesis and Department of Chemistry, Sogang University, Seoul 121-742, Korea.

*To whom correspondence should be addressed. E-mail: yoonkb@sogang.ac.kr